Paper draft v1.9 for supersat project

K. Latimer

June 2, 2021

Questions/comments from DR in blue
Responses from KL in red
Hanging details to address before final draft

1   Intro

In a recent paper, Fan et al introduce a novel "warm phase invigoration mechanism" (WPIM) in which increased concentrations of ultrafine aerosol particles ($UAP_{<50}$, with 50 signifying an upper bound on particle diameter of 50nm) in the boundary layer (BL) result in enhanced convective updraft speeds and precipitation rates [1]. As pointed out by Grabowski and Morrison, the precise explanation for this physical effect is that, in allowing for lower equilibrium water vapor supersaturation (SS) values in rising convective parcels, these excess aerosol particles lead to an increase in the buoyancy of the parcel over the course of its ascent, thus enhancing convective speeds [2].

In order to get a quantitative intuition for how this works, we offer a simplified version of the calculation in [3], which still conveys the same essential idea. We consider a polluted (non-supersaturated; i.e. $RH = 1$) storm ascending in an environment whose temperature profile has been set by clean storms. The parcel condenses water vapor as it rises, and for simplicity we assume no latent heat is lost to the environment. We then have (see Table 1 for explanation of constants and variables used in the text. We use δ here to represent a variation in state variables between two parcels, as distinguised from d in Equation 5 which denotes a proper differential form):

$$C_{ap}\delta T + L_v\delta q_v = 0, \tag{1}$$

where q_v is the water vapor mass fraction of the parcel ($q_v = m_v/m_{tot}$), also expressed in terms of the the relative humidity (RH) and saturation water vapor mass fraction (q_v^*) as:

$$q_v = RHq_v^* \tag{2}$$

Usig the Clausius-Clayperon equation:

$$\delta q_v^* = \delta\Big(\frac{e_s V}{R_v T m_{tot}}\Big)$$
$$= \frac{\delta e_s}{e_s}q_v^* - \frac{\delta T}{T}q_v^*$$
$$= \frac{L_v \delta T}{R_v T^2}q_v^* - \frac{\delta T}{T}q_v^*$$
$$= \Big(\frac{L_v}{R_v T} - 1\Big)\frac{\delta T}{T}q_v^*$$
$$\approx \frac{q_v^* L_v}{R_v T^2}\delta T \tag{3}$$

Taking the differential of Equation 2 and rearranging terms in Equations 1, 2, and 3 yields:

$$\delta T = \frac{-L_v q_v^*}{C_{pa} + q_v \frac{L_v^2}{R_v T^2}}\delta RH \tag{4}$$

Plugging in typical values for RH (≈ 1.1) and T (≈ 300 K) gives $\delta T \approx 1$ K.

In their paper (see for example Figure 2(b) of that work), Fan et al provide anecdotal evidence that the WPIM is capable of producing enhancements in vertical wind velocity on the order of 10 m/s for polluted relative to unpolluted storms. Even neglecting diffusive, frictional, or radiative losses, this requires a variation in convective available potential energy ($CAPE$) of ≈ 100 J/kg, or a RH difference between the dirty storm and clean environment of ≈ 0.1, i.e., the environment must support SS on the order of 10% throughout the troposphere.

While Fan et al do not offer any proof based on experimental data that such high SS exist in the convection setting the environmental lapse rate, they do observe comparable values in numerical simulations. In particular, using the Weather Research and Forcasting (WRF) model to simulate pristine (no UAP$_{<50}$) conditions in the Amazon Rainforest, they find (horizontally- and time-averaged) SS in convective cores of up to 15%.

Since this is well above what is typically reported or assumed in the literature [4, 5, 6, 7, 8, 9, 10, 11, 12], we seek in this paper to determine if we can find experimental evidence for O(10%) SS in nature. We use data from the High-Altitude LOng-range research aircraft (HALO) (part of the ACRIDICON-CHUVA mission in and around Manaus, Brazil in 2014-15).

2 Data Analysis and Results

In order to determine experimental supersaturation within a reasonable margin of error, we must use the quasi-steady-state supersaturation (SS_{QSS}) formula [13]. In order to determine the region of validity for this approximation, we used data from the WRF output, since this allows us to compare to the true supersaturation (here called SS_{WRF}). We focused on the following considerations:

- The QSS approximation should be a good and reliable estimate for the actual SS, i.e. least-squares linear regression slope and correlation coefficients ≈1.

- We want the criteria to be inclusive enough that we are still capturing a significant fraction of the convection which sets the average temperature profile of the troposphere.

- In keeping with the analysis by Fan et al, and with our general interest in studying convective cores, we additionally exclude the w lower bound value of 0 to ensure we are capturing reasonably strong updrafts.

In Figure 1 we synthesize the data needed to take all three of the above considerations into account. We find that taking $LWC > 10^{-4}$ kg/kg and $w > 1$ m/s yields the best agreement of the QSS approxiamtion with the true SS while still yielding a subset of the data that accounts for greater than half of the condensational latent heating in the troposphere below the freezing line and consists of reasonably strong convective updrafts. To summarize, we use the following criteria in all subsequent analyses:

- T >273K (we're not including ice in the theory; note that Fan et al do evaluate SS wrt water above the freezing line though)

- w >1 m/s

- cloud LWC >1e-4 g/g (in the convection core)

- including rain droplets and ventillation corrections

We would like to further quantify the spread of true SS values for a given value predicted by the QSS approximation. In Figure 2, we plot a range of quantiles for the true SS given the predicted SS, using the polluted and unpolluted data sets combined (see Table **??** for details on the regression parameters for each case).

In their analysis, Fan et al use the following filtering criteria:

- For experimental data: They examine the upper 10th percentile of updrafts in "convective events" which 1) Fall between 11h00 and 19h00 local time 2) Have no other convective events occuring at any point in time 3 hours prior, and 3) Have max echo height at >0dBz above 10km. For aerosol measurements they take the average of measurements in the 30-min interval prior to the convective event. The authors do not state their criteria for what qualifies as a convective event.

- For model data: They limit analysis to a subset of the horizontal domain (red box in Fig S8) that encompasses a single convective event during the day of the simulation. They again take the top 10th percentile of updrafts with $w > 2$.

Because we use slightly different filtering criteria than that described above, we first verify that the data points selected by our filter yield similar SS profiles in the WRF simulation as those found in the latter work. In Figure 3 we plot vertical SS profiles for all filtered data points, as well as for the upper 10 percentiles of all fitered data points. We define the points in the "upper 10 percentiles" as those with w greater than the 90th-percentile (out of all altitudes and times) vertical wind velocity. Data in Figure 3 are binned according to the simulation grid, which is based on pressure coordinates so that bin size varies logarithmically with respect to z. For this and future vertical profiles, the vertical coordinate of plotted points represents the average over all vertical coordinates of points in the corresponding bins. In [1] they consider a restricted subdomain around the T3 field station, indicated in Figure S8 of the supplementary information for that paper; we do not see a major qualitative difference when including this additional criterion; see Figure 15. We do indeed find the high SS values reported by Fan et al (maximum values of 13% in both polluted and unpolluted cases from the upper 10th percentile dataset), confirming that our filtering criteria establish a fair basis for comparison here.
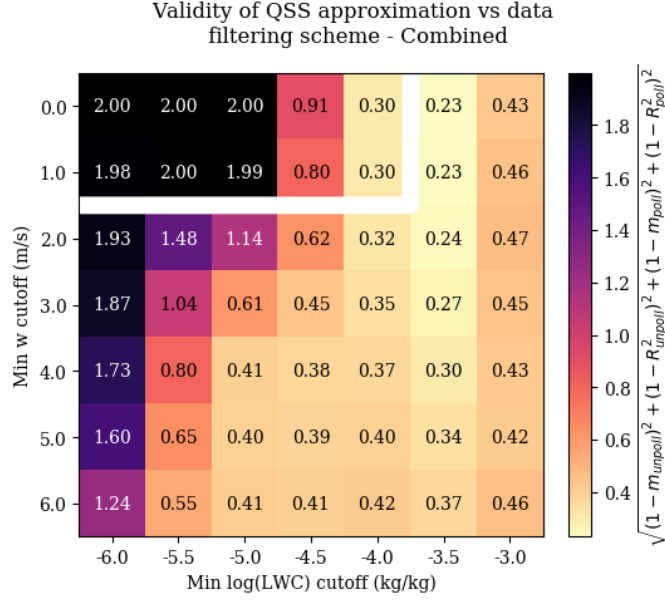
4

Validity of QSS approximation vs data
filtering scheme - Combined

Min w cutoff (m/s) \ Min log(LWC) cutoff (kg/kg)	-6.0	-5.5	-5.0	-4.5	-4.0	-3.5	-3.0
0.0	2.00	2.00	2.00	0.91	0.30	0.23	0.43
1.0	1.98	2.00	1.99	0.80	0.30	0.23	0.46
2.0	1.93	1.48	1.14	0.62	0.32	0.24	0.47
3.0	1.87	1.04	0.61	0.45	0.35	0.27	0.45
4.0	1.73	0.80	0.41	0.38	0.37	0.30	0.43
5.0	1.60	0.65	0.40	0.39	0.40	0.34	0.42
6.0	1.24	0.55	0.41	0.41	0.42	0.37	0.46

Colorbar label: $\sqrt{(1-m_{unpoll})^2 + (1-R^2_{unpoll})^2 + (1-m_{poll})^2 + (1-R^2_{poll})^2}$

Figure 1: Systematic evaluation of data filtering scheme using WRF model outputs. Here, the heatmap color corresponds to the Euclidean distance in the 4-dimensional space of tuples $(m_{poll}, R^2_{poll}, m_{unpoll}, R^2_{unpoll})$ from the ideal point $(1, 1, 1, 1)$, where subscripts 'poll' and 'unpoll' correspond to Fan et al's 'C_PI' (polluted) and 'C_BG' (unpolluted) model scenarios, respectively. Numerical values of this distance are also given as annotations to aid in distinguishing similar colors. Values on the horizontal and vertical axes represent, respectively, minimum LWC and w cutoffs used to filter WRF simulation data. In all cases we additionally restrict our consideration to points with temperature above 273 K. We also seek to evaluate the fraction of domain-wide positive (i.e. condensational) latent heating attributed to points selected through the data filter. The higher the fraction, the more confidence we have (in an unquantified sense) that we are capturing a complete picture of the convection which sets the temperature profile in the troposphere. The white contour line indicates the region of the heatmap where the LH fraction is $> 50\%$ for both polluted and unpolluted model scenarios.
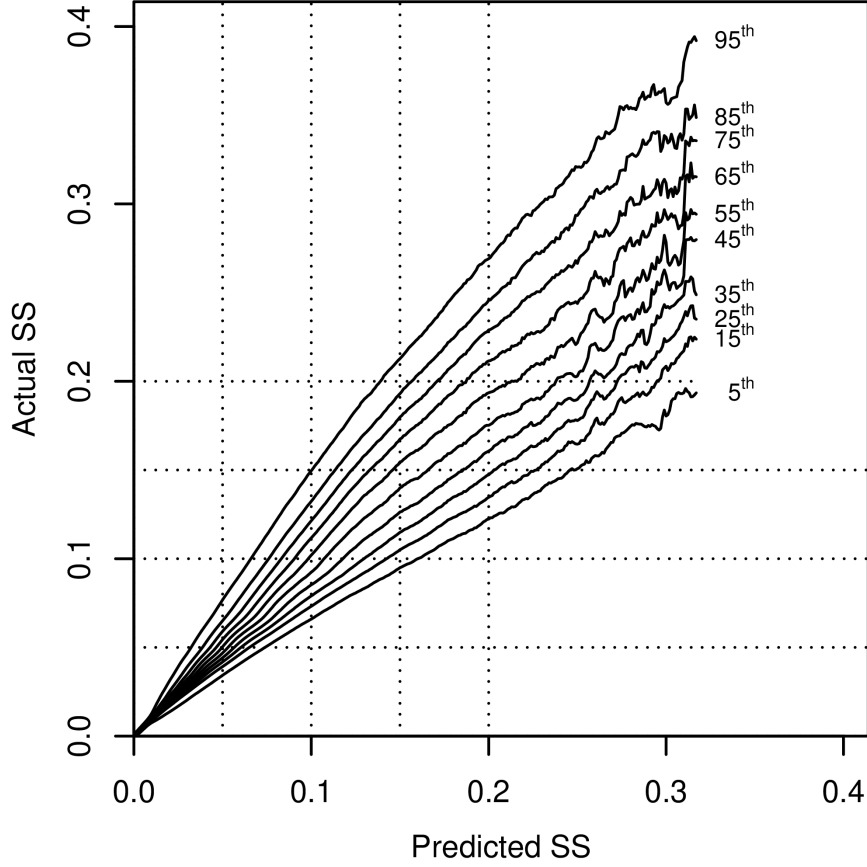
Figure 2: This figure shows the spread of true SS values for a given value predicted by the QSS approximation, using the combined WRF output from both polluted and unpolluted models. Each curve follows a fixed quantile (labeled on the figure) across the domain of predicted SS values for the range of actual SS. The quantiles are calculated with a 0.01-wide moving window centered on the respective predicted value. We see that the actual SS hew closely enough to the predicted SS that a high predicted SS guarantees a high actual SS, and vice versa. Up to about a QSS SS of 0.1, the median actual SS is, to good approximation, equal to the predicted SS. From this plot we can simply read off the confidence level of our lower bound on actual SS; for example, for a single predicted SS of 0.1, there is 95% confidence that actual SS < 0.15.

Supersaturation and area fraction vertical profiles - WRF
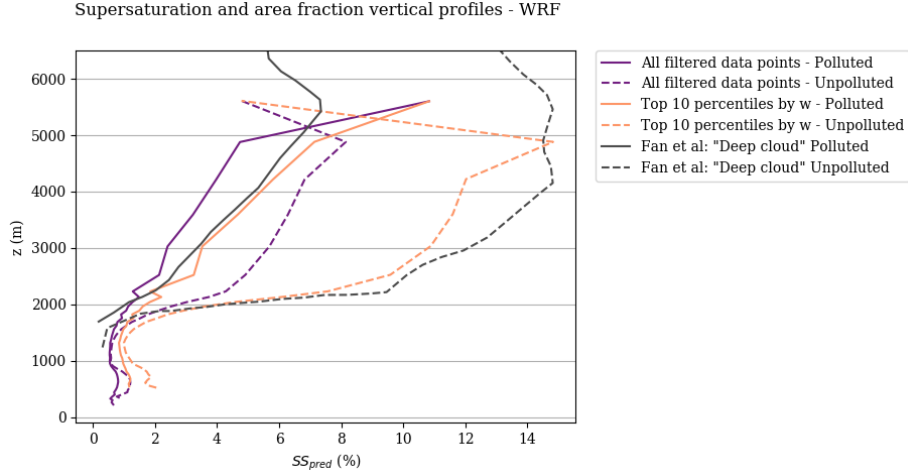
Figure 3: [*This figure is too busy for the one point it is trying to make. Just show the two curves in panel "left a" and the black and orange curves in "left b", possibly all in the same plot. I realize I didn't state this explicitly in the figure, but the right panels do show that the majority of points lie in regions where the supersaturation is relatively low. Do you not think this is an important thing to point out? I do not think so. The distribution in the b panels is a combination of where the plane flew (definitely not of physical interest) and the mass-flux profile (which could decline with height starting a bit above the cloud base). Even if the observational sampling were unbiased, our point is that SS is low everywhere below the melting line, not just near the cloud base. OK. Just to clarify, these are the simulation data so there's no plane flying. But I think I take your general point and have modified the figure accordingly.*] This figure serves to verify that our data filtering scheme yields SS profiles similar to those obtained by Fan et al (c.f. Figure 4 of that paper). Using all filtered data points (purple) and only the top 10 percentiles of filtered data points as measured by w (orange; see text for details), the latter being aligned with the analysis method of Fan et al. Profiles show SS_{pred} averaged across time and horizontal spatial coordinates. Note that z interval width scales logarithmically with z, in accordance with the WRF grid spacing. The gray curves are reconstructed from [1]. We observe that our filtering scheme indeed recovers average SS_{QSS} values on the order of 10% as reported in [1].

7

We now seek to determine whether such high values actually occur in nature. First we look at data from the HALO flights in September and October of 2014 (see Methods/SI for details on selection of dates for this analysis) [*find citation*]. Figure 4 shows the analogue of Figure 3 using data from all HALO flight dates combined. We find no points with average SS above 1 %, even when limiting to the strongest updrafts in the combined dataset.
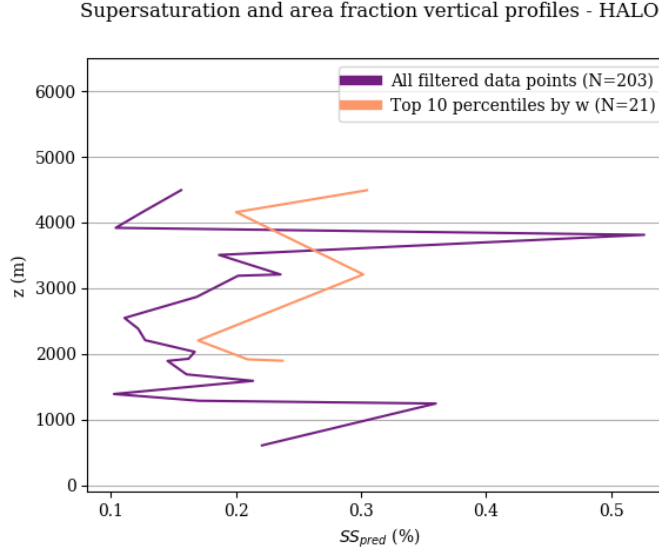

Supersaturation and area fraction vertical profiles - HALO

Figure 4: This figure serves to determine whether the high-SS values found in the WRF simulation output indeed occur in nature. Profile shows SS_{pred} averaged across all filtered data points (purple) from HALO flight campaign (all dates combined), as well as across only the top 10 percentiles of those filtered data points as measured by w (orange; see text for details). We do not find any points in the SS_{pred} profile with values above 1%, even when restricting to only the top 10 percentiles.

We can use Equation 4 and the SS profiles in Figures 3 and 4 to infer a buoyancy profile for a hypothetical non-supersaturated parcel. For this analysis we take the temperature of the parcel equal to that of the environment (i.e., what has been measured). The resulting error in the value of δT in Equation 5 is quadratic in δRH, which is acceptable for our purposes. In Figure 5 we plot δT profiles from both WRF simulations and field campaigns side-by-side. We use these profiles to derive enhancements in $CAPE$ for the non-supersaturated parcel as:

$$\delta CAPE = g \int dz \frac{\delta T}{T} \tag{5}$$

where we again approximate T as the environmental temperature and integrate from 647 to 4488 m, the common vertical domain for all four curves in Figure 5.

8

We find values of $\delta CAPE$ of 2, 25, and 50 J/kg for HALO, WRF (polluted), and WRF (unpolluted), respectively. Neglecting any other physical energy sinks as above, these translate to vertical velocity enhancements on the order of 1 m/s in the field campaign and 10 m/s in both the simulations under consideration.

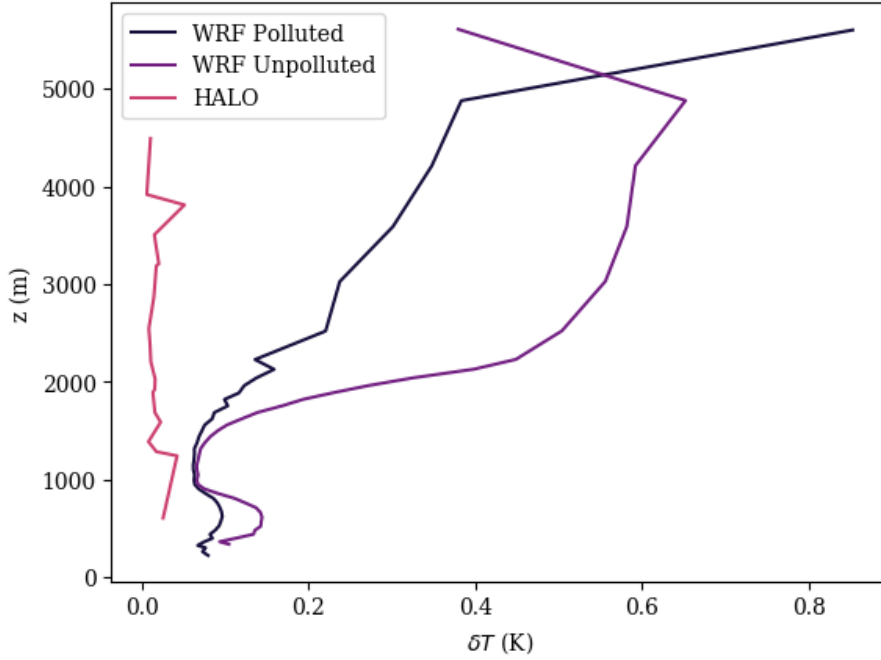Buoyancy profiles derived from simple parcel model

Figure 5: Profiles for δT of a non-supersaturated ($RH = 1$) parcel ascending in an environment with SS profiles shown in Figures 3-**??**, using Equation 5. We find that the buoyancy of this hypothetical parcel in nature is far lower than in the simulations, casting doubt on the real validity of the WPIM as described in Fan et al.

One possible counterargument is that the aerosol concentrations in the BL during the dates of the HALO flights might have been significantly higher than those during the dates considered in Fan's paper, thus precluding the occurence of high SS values in the troposphere. In order to investigate this, we use the aerosol particle size distribution measured by the scanning mobility particle sizer (SMPS) in Manacapuru, located southwest of Manaus (PI: Chongai Kuang). This intrument measures particle concentrations in the diameter range 11.1-469.8nm. In Figure 6, we show that, while we do indeed see higher total aerosol concentrations on average during the HALO flight date range (3500/ccm vs 2400/ccm), the UAP50 concentration is on average lower

(670/ccm vs 1600/ccm). In fact, the aerosol concentrations used in the WRF simulations are much lower than those observed during the day the simulation takes place, which is not justified quantitatively in that study.

We note additionally that the positive experimental correlation between concentration of UAP50 and maximum vertical velocity during the dates studied by Fan et al is not significant at the 95% confidence level - the least-squares slope parameter for their data set has a p-value of 0.11.

Another possible counterargument is that the flight campaigns simply didn't fly through strong enough updrafts. However the vertical velocity distributions from the campaigns are quite similar to that from the simulations. See Figure 7.

Conclusion: The WPIM as proposed by Fan et al requires the average temperature profile of the troposphere to be set by relatively clean (high-SS) convection, in order for more polluted (low-SS) convection to experience an enhancement in buoyancy. However, we find no evidence that the high SS values reported by Fan's model actually occur in nature, which weakens the possibility of measureable invigoration effects - in particular, we estimate an upper bound on vertical velocity enhancement of ≈ 1 m/s from the HALO flight campaign, compared to ≈ 10 m/s from Fan's control simulations in WRF. The relatively low aerosol concentrations used to initialize the simulations, in combination with possible irregularities in microphysical parameterizations, may be to blame for the anomalously high SS values in the WRF output.

Aerosol concentration distributions - 11.1-469.8 nm

(a)

Aerosol concentration distributions - 11.1-50 nm
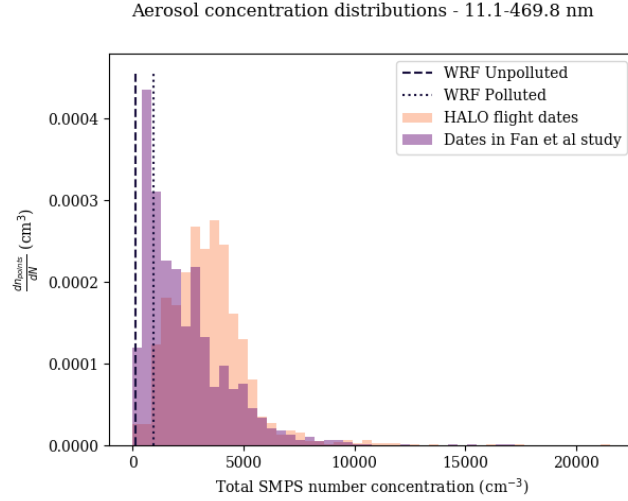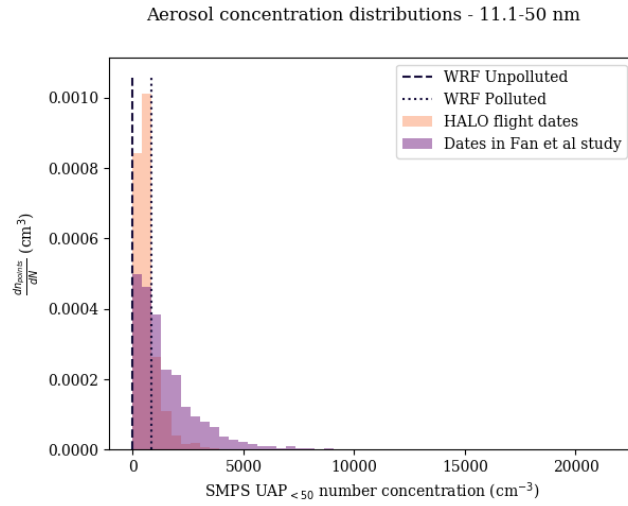
(b)

Figure 6: Distribution of aerosol concentration measurements by the ground-based SMPS at Manacapuru, Brazil; a) entire size range, b) only particles with diameter greater than 50nm. HALO flight dates are the same as those represented in Figure 4 (see main text for details). Dashed (dotted) lines show initial concentrations in the BL of the WRF simulation of polluted (unpolluted) conditions. The unpolluted model aerosol concentrations are quite low relative to what is actually observed.

Vertical wind velocity distributions
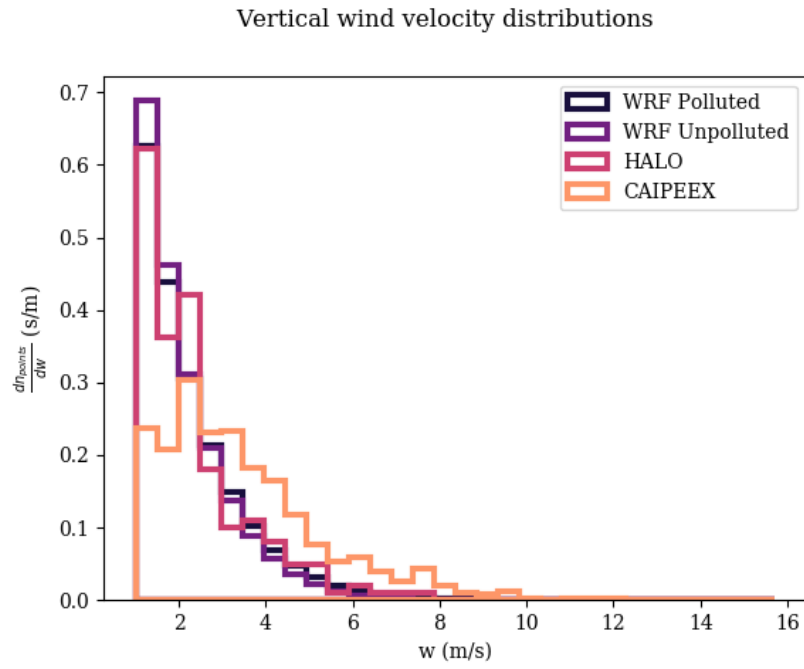
Figure 7: Vertical wind velocity probability distributions from simulations and field campaigns, using filtering criteria outlined in the text. Experimental distributions are not qualtitatively different from those in the simulation.

3 Methods

3.1 WRF

Model output for control simulations of polluted ("C_BG") and unpolluted ("C_PI") scenarios were provided by Fan et al; see that paper and accompanying SI for detailed explanations of model parameters and initializations.

In this paper, we use the following form of the QSS SS equation after [13] (with SS_{QSS} given as a percentage):

$$SS_{QSS} = \frac{A(T)w}{4\pi B(\rho_a, T)\langle f(r) \cdot r\rangle n} * 100, \tag{6}$$

where:

$$A(T) = \frac{g}{R_a T}\left(\frac{L_v R_a}{C_{ap} R_v T} - 1\right)\left(F_d(T) + F_k(T)\right)$$

$$F_d(T) = \frac{\rho_w R_v T}{D e_s(T)}$$

$$F_k(T) = \left(\frac{L_v}{R_v T} - 1\right)\frac{L_v \rho_w}{KT}$$

$$B(\rho_a, T) = \rho_w\left(\frac{R_v T}{e_s(T)} + \frac{L_v^2}{R_v C_{ap} \rho_a T^2}\right) \tag{7}$$

Notation for constants and variables is given in Table 1. We use the following parameterization for e_s [13]:

$$e_s(T) = 611.2 e^{\frac{17.67 T_c}{T_c + 243.5}}, \tag{8}$$

where T_c is the temperature in degrees Celsius.

We note that this equation by also include finite size correction terms; however, using typical values for droplet salinity and condensation nucleus radius (the relevant parameters in this case), these terms are insignificant ($< 0.1\%$ correction to SS) for drops of radius greater than 3 μm [13], and we therefore do not consider them in this paper.

A simpler form of Equation 6 is often employed in the literature [2, 13], with:

$$A(T) = \frac{g}{R_a T}\left(\frac{L_v R_a}{C_{ap} R_v T} - 1\right)$$

$$B(T) = D \tag{9}$$

Figure 10 shows that this form does not yield as good of agreement with the actual SS reported in WRF.

We use the expressions given in [14] and [13] for ventilation corrections, which are quite extensive. Full formulae are contained in the analysis code at this GitHub repo. Figures 11 and 12 show, respectively, the effects of neglecting these corrections (i.e. setting $f(r) = 1$ for all r) for rain drops (defined here as liquid water drops with radius greater than 102 μm), and omitting rain drops altogether from the calculations of mean radius and number concentration.

3.2 HALO

The HALO aircraft supported two instruments for measuring cloud droplet spectra: a cloud and aerosol spectrometer (CAS-DPOL) and a cloud droplet probe (one element of a cloud combination probe) (CCP-CDP) [15]. We found that the CCP-CDP consistently reported unphysical bimodal size distributions, and therefore used only data from the CAS-DPOL for all calculations involving cloud droplets. Number concentrations from the CAS-DPOL were corrected using the ξ factor derived in [16].

The rain drop spectra came from data collected by greyscale cloud imaging probe (second element of the cloud combination probe) (CCP-CIP). The drop diameter detection ranges for CAS-DPOL and CCP-CIP were 0.89-50 μm and 25-2000 μm, respectively. Per guidance from the principal investigators for the CAS-DPOL, we only included data for droplets from size bins with a lower diameter bound greater than or equal to 3 μm in the analysis [17].

There was some ambiguity in how to treat the region of overlap of the CAS-DPOL and the CCP-CIP instruments. Upon examination of spectra across the range of dates in question, we see that the first size bin for CCP-CIP consistently reports suspect measurements. For example, correlation in number concentrations measured by this bin with those measured by neighboring bins is consistently low (Figure 13), and there are a relatively high number of instances where the spectrum shows an unphysical spike for that bin (Figure 14). We therefore apply the average value of $\frac{dN}{dlogDp}$ for all CAS-DPOL bins in the range of 25-50 μm diameter across the entire region of 25-75 μm diameter (namely the range of CCP-CIP bin 1).

All measurements of environmental variables were taken from the Basic Halo Measurement and Sensor System (BAHAMAS).

Out of the dates for which all three instruments (BAHAMAS, CAS-DPOL, CCP-CIP) report data, we take those for which measurements of shared variables (true airspeed for BAHAMAS and CAS-DPOL; ξ correction factor for CAS-DPOL and CCP-CIP) are well-correlated (R^2 above 0.95). These are (all in 2014): 6, 9, 11, 12, 16, 18, 27, 28, 30 September; 1 October.

We used the same Equation 6 for SS_{QSS} and for ventilation factors as described above.

14

4 Supplementary

Symbol	Meaning	Value of constant	Notes
C_{ap}	Specific heat capacity at constant pressure, dry air	1005 J/kg	We take as constant wrt T
D	Molecular diffusion constant of water in dry air	0.23e-4 m^2/s	-
e_s	Saturation vapor pressure, water	-	
$f(r)$	Ventilation factor	-	
g	Gravitational acceleration on Earth	9.8 m/s	We take as constant wrt T
K	Coefficient of thermal conductivity in dry air	2.4e-2 J/(m s K)	
LWC	Liquid water content	-	
L_v	Latent heat of vaporization, water	2.501e6 J/kg	We take as constant wrt T
N	Particle number concentration	-	
n_{points}	Point probability density	-	
q_v	Water vapor mass mixing ratio	-	Equals $\frac{m_v}{m_{tot}}$
q_v^*	Saturation water vapor mass mixing ratio	-	Equals $\frac{m_v^*}{m_{tot}}$
r	Particle radius	-	
RH	Relative humidity	-	Equals $SS+1$
ρ_a	Mass density, dry air	-	Assuming ideal gas law
ρ_w	Mass density, liquid water	1000 kg/m^3	
R_a	Ideal gas constant, dry air	287.19 J/(kg K)	
R_v	Ideal gas constant, water	460.52 J/(kg K)	
SS	Supersaturation	-	Equals $RH-1$
T	Temperature	-	
T_c	Temperature in degrees C	-	Equals $T-273.15$
w	Vertical wind velocity	-	
z	Altitude	-	

Table 1: Explanation of constants and variables used in the paper.
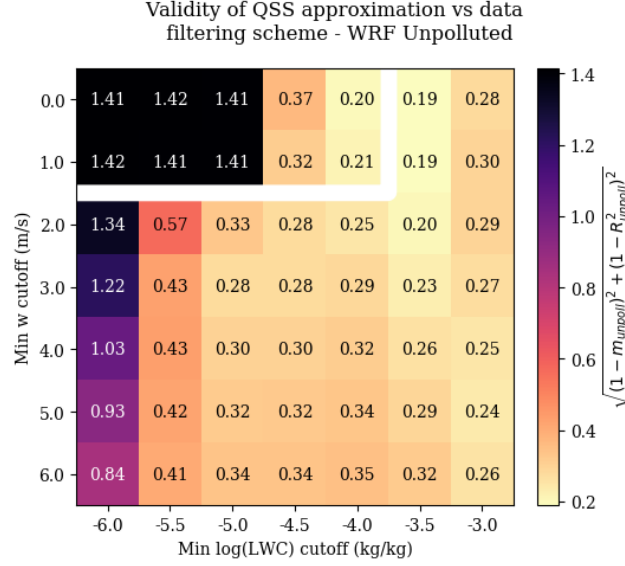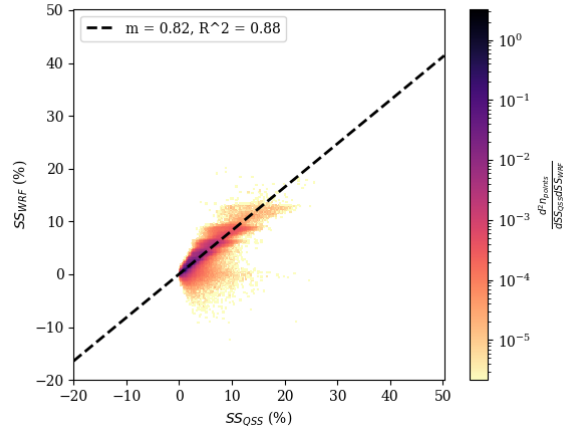
(a) Unpolluted case.
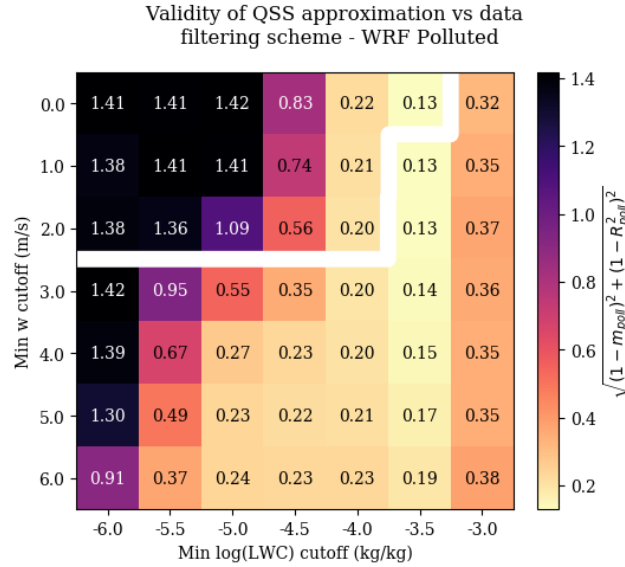
(b) Polluted case.

Figure 8: Heatmaps used to evaluate regime in which the QSS approximation gives a good estimate for the true SS. The parameters used to judge the quality of this estimate are the least-squares linear regression slope m and correlation coefficient R^2 when plotting the true SS output from the simulation data (SS_{WRF}) versus the value derived from the WSS formula (SS_{QSS}) - see methods section. Values on the horizontal and vertical axes represent, respectively, minimum LWC and w cutoffs used to filter WRF simulation data. In all cases we additionally restrict our consideration to points with temperature above 273 K. Results are shown for model runs labeled in Fan et al as a) 'C_PI' (Unpolluted; subscript 'unpoll') and b) 'C_BG' (Polluted; subscript 'poll').

Actual versus approximated supersaturation - WRF Unpolluted
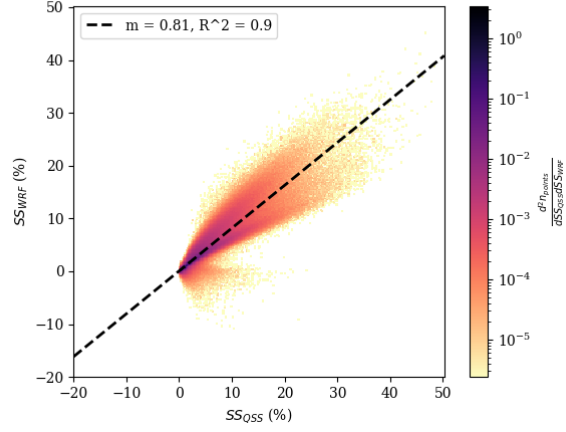
(a) Unpolluted case.

Actual versus approximated supersaturation - WRF Polluted
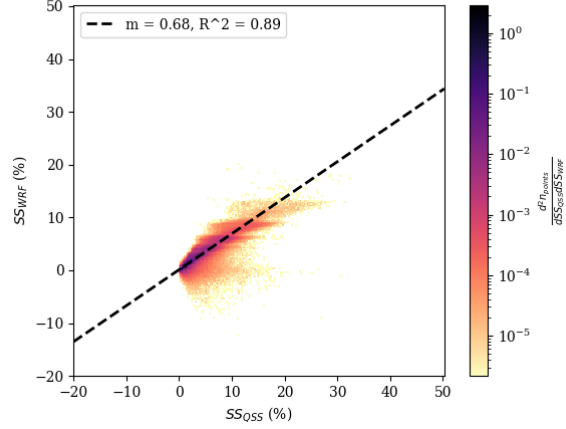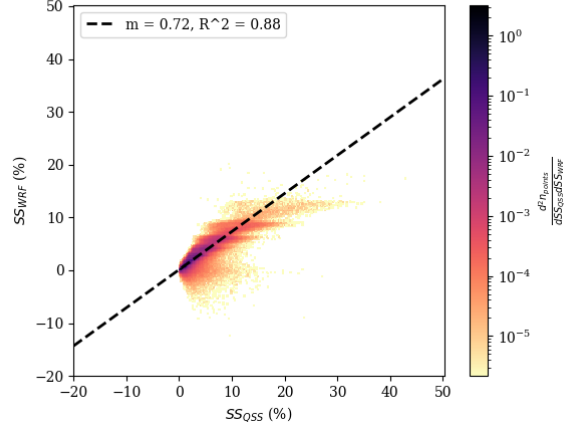

(b) Polluted case.

Figure 9: Plot of SS_{QSS} versus SS_{WRF} using the filtering scheme described in the main text. Dashed line shows the fit from least-squares linear regression. Color denotes the density of data points; note the scale is logarithmic in this figure. The majority of points are clustered near the origin.

Actual versus approximated supersaturation - WRF Unpolluted
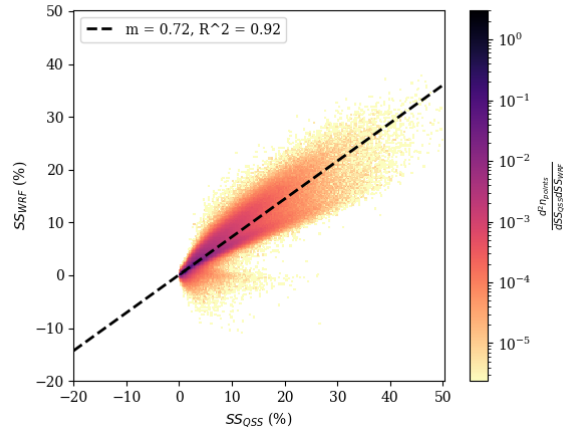
(a) Unpolluted case.

Actual versus approximated supersaturation - WRF Polluted

(b) Polluted case.

Figure 10: Same as Figure 9, using simplified form of Equation 6. Correlation is not appreciably affected but the value of least-squares linear regression slopes is lower for both simulation cases.
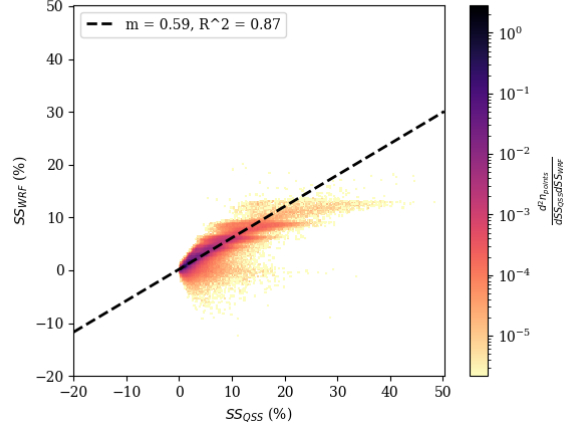
(a) Unpolluted case.

(b) Polluted case.

Figure 11: Same as Figure 9, without ventilation corrections. Correlation is not appreciably affected but the value of least-squared linear regression slopes is lower for both simulation cases.

Actual versus approximated supersaturation - WRF Unpolluted
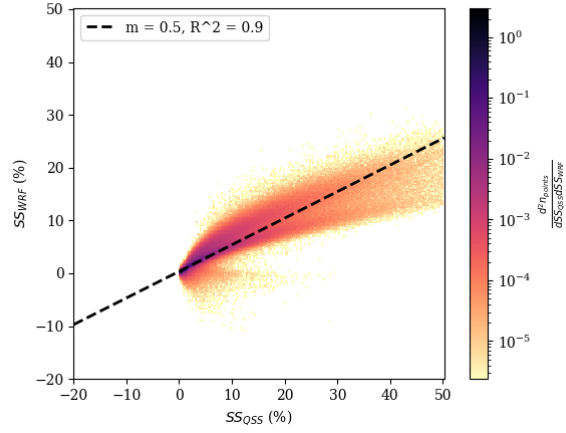
(a) Unpolluted case.

Actual versus approximated supersaturation - WRF Polluted

(b) Polluted case.

Figure 12: Same as Figure 9, without contributions from rain drops. Correlation is slightly lower and the value of least-squared linear regression slopes is lower for both simulation cases.
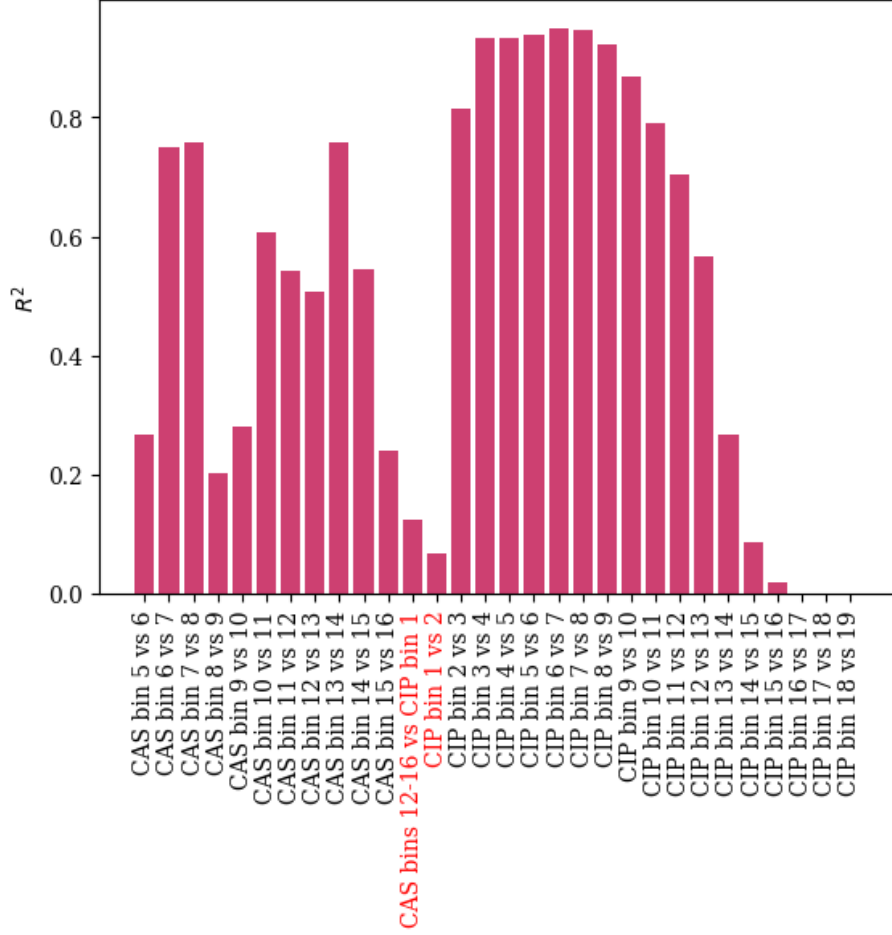
Figure 13: Correlation coefficient for number concentrations measured in adjacent or overlapping bins. We find that number concentrations measured by CCP-CIP bin 1 (25-75 μm diameter) correlate poorly with those measured by CAS bins 12-16 (25-50 μm diameter) and by CIP bin 2 (75-125 μm diameter), indicating discontinuity with the rest of the drop size distribution at that point. The very low correlations at the upper end of the total size range are due to the fact that number concentrations in that regime are very close to zero for all times and therefore are essentially noise.
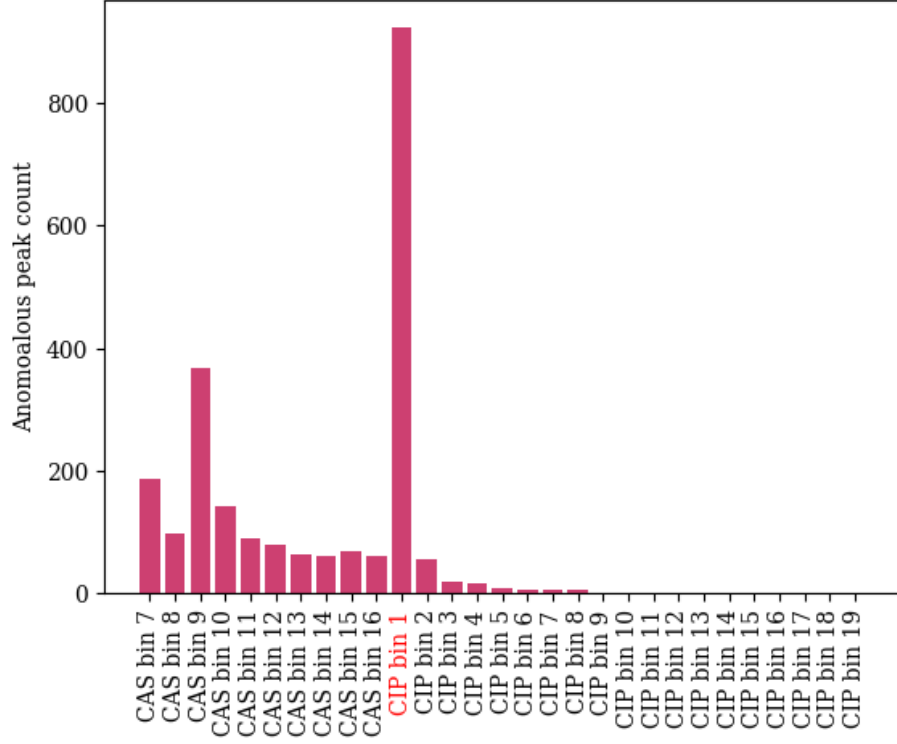
Figure 14: Raw count of samples across all dates under consideration where $\frac{dN}{dlogDp}$ measured by a given bin is a global maximum for the spectrum and also greater than 5 times the next highest bin's $\frac{dN}{dlogDp}$ in that same spectrum. This figure shows that the measured spectrum often has a spike at CIP bin 1, which we believe is unphysical.

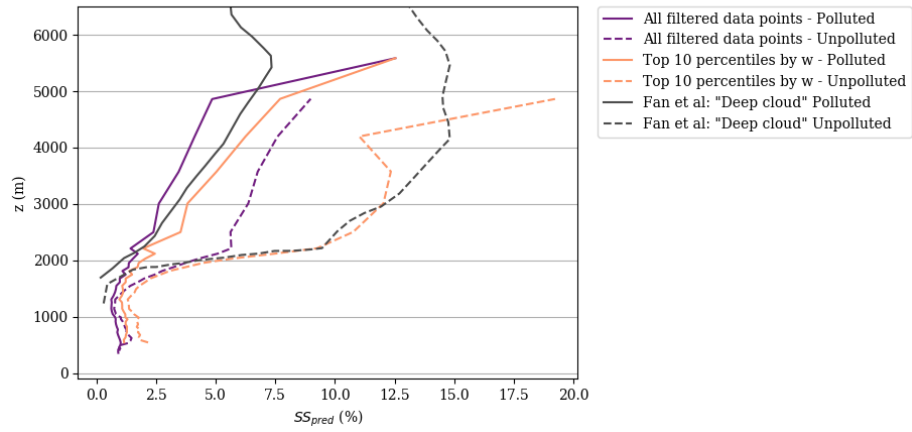Supersaturation and area fraction vertical profiles - WRF (subdomain)

Figure 15: Analagous to Figure 3, restricted to the horizontal subdomain indicated by the red box in Figure S8 of Fan et al (bottom left panel). Qualitatively the results are quite similar, suggesting that the restriction to this subdomain is not crucial to the results described in Fan's paper.

References

[1] J. Fan, D. Rosenfeld, Y. Zhang, S. E. Giangrande, Z. Li, L. A. T. Machado, S. T. Martin, Y. Yang, J. Wang, P. Artaxo, H. M. J. Barbosa, R. C. Braga, J. M. Comstock, Z. Feng, W. Gao, H. B. Gomes, F. Mei, C. Pöhlker, M. L. Pöhlker, U. Pöschl, and R. A. F. de Souza, "Substantial convection and precipitation enhancements by ultrafine aerosol particles," *Science*, vol. 359, pp. 411–418, 1 2018.

[2] W. W. Grabowski and H. Morrison, "Do ultrafine cloud condensation nuclei invigorate deep convection?," *Journal of the Atmospheric Sciences*, vol. 77, pp. 2567–2583, 7 2020.

[3] W. W. Grabowski and D. Jarecka, "Modeling condensation in shallow non-precipitating convection," *Journal of the Atmospheric Sciences*, vol. 72, pp. 4661–4679, 12 2015.

[4] W. A. Hoppel, G. M. Frick, and J. W. Fitzgerald, "Deducing droplet concentration and supersaturation in marine boundary layer clouds from surface aerosol measurements," *Journal of Geophysical Research: Atmospheres*, vol. 101, pp. 26553–26565, 11 1996.

[5] F. Yang, R. McGraw, E. P. Luke, D. Zhang, P. Kollias, and A. M. Vogelmann, "A new approach to estimate supersaturation fluctuations in stratocumulus cloud using ground-based remote-sensing measurements," *Atmospheric Measurement Techniques*, vol. 12, pp. 5817–5828, 11 2019.

[6] M. Koike, N. Takegawa, N. Moteki, Y. Kondo, H. Nakamura, K. Kita, H. Matsui, N. Oshima, M. Kajino, and T. Y. Nakajima, "Measurements of regional-scale aerosol impacts on cloud microphysics over the east china sea: Possible influences of warm sea surface temperature over the kuroshio ocean current," *Journal of Geophysical Research: Atmospheres*, vol. 117, pp. n/a–n/a, 9 2012.

[7] M. K. Politovich and W. A. Cooper, "Variability of the supersaturation in cumulus clouds," *Journal of the Atmospheric Sciences*, vol. 45, pp. 1651–1664, 6 1988.

[8] N. Moteki, T. Mori, H. Matsui, and S. Ohata, "Observational constraint of in-cloud supersaturation for simulations of aerosol rainout in atmospheric models," *npj Climate and Atmospheric Science*, vol. 2, 12 2019.

[9] H. Siebert and R. A. Shaw, "Supersaturation fluctuations during the early stage of cumulus formation," *Journal of the Atmospheric Sciences*, vol. 74, pp. 975–988, 4 2017.

[10] C. Shen, C. Zhao, N. Ma, J. Tao, G. Zhao, Y. Yu, and Y. Kuang, "Method to estimate water vapor supersaturation in the ambient activation process using aerosol and droplet measurement data," *Journal of Geophysical Research: Atmospheres*, vol. 123, 9 2018.

[11] E. Hammer, N. Bukowiecki, M. Gysel, Z. Jurányi, C. R. Hoyle, R. Vogt, U. Baltensperger, and E. Weingartner, "Investigation of the effective peak supersaturation for liquid-phase clouds at the high-alpine site jungfraujoch, switzerland (3580 m a.s.l.)," *Atmospheric Chemistry and Physics*, vol. 14, pp. 1123–1139, 1 2014.

[12] X.-Y. Li, G. Svensson, A. Brandenburg, and N. E. L. Haugen, "Cloud-droplet growth due to supersaturation fluctuations in stratiform clouds," *Atmospheric Chemistry and Physics*, vol. 19, pp. 639–648, 1 2019.

[13] R. R. Rogers and M. K. Yau, *A Short Course in Cloud Physics*. Butterworth Heinemann, 3 ed., 1989.

[14] H. Pruppacher and J. Klett, *Microphysics of Clouds and Precipitation*. Springer Netherlands, 2010.

[15] R. C. Braga, D. Rosenfeld, R. Weigel, T. Jurkat, M. O. Andreae, M. Wendisch, M. L. Pöhlker, T. Klimach, U. Pöschl, C. Pöhlker, C. Voigt, C. Mahnke, S. Borrmann, R. I. Albrecht, S. Molleker, D. A. Vila, L. A. T. Machado, and P. Artaxo, "Comparing parameterized versus measured microphysical properties of tropical convective cloud bases during the acridicon–chuva campaign," *Atmospheric Chemistry and Physics*, vol. 17, pp. 7365–7386, 6 2017.

[16] R. Weigel, P. Spichtinger, C. Mahnke, M. Klingebiel, A. Afchine, A. Petzold, M. Krämer, A. Costa, S. Molleker, P. Reutter, M. Szakáll, M. Port, L. Grulich, T. Jurkat, A. Minikin, and S. Borrmann, "Thermodynamic correction of particle concentrations measured by underwing probes on fast-flying aircraft," *Atmospheric Measurement Techniques*, vol. 9, pp. 5135–5162, 10 2016.

[17] T. Jurkat, R. Weigel, and C. Mahnke, "Private correspondence," 2020.